Published online 18 July 2019

Nucleic Acids Research, 2019, Vol. 47, No. 17 ***e100***
doi: 10.1093/nar/gkz609

Ultra-soft X-ray system for imaging the early cellular responses to X-ray induced DNA damage

Jakub A. Kochan[1,2], Matthias van den Belt[1], Julia von der Lippe[1], Emilie C.B. Desclos[1], Barbara Steurer[3], Ron A. Hoebe[1], Enzo M. Scutigliani[1], Jan Verhoeven[1], Jan Stap[1], Ruben Bosch[1], Meindert Rijpkema[1], Carel van Oven[1], Henk A. van Veen[1], Irene Stellingwerf[1], Lianne E.M. Vriend[1], Jurgen A. Marteijn[3], Jacob A. Aten[1] and Przemek M. Krawczyk[1,*]

[1]Department of Medical Biology, Amsterdam University Medical Centers (location AMC), Cancer Center Amsterdam, Meibergdreef 15, 1105 AZ Amsterdam, The Netherlands, [2]Department of Cell Biochemistry, Faculty of Biochemistry, Biophysics and Biotechnology, Jagiellonian University, 30-387 Krakow, Poland and [3]Erasmus MC, University Medical Center Rotterdam, Department of Molecular Genetics, Oncode Institute, Wytemaweg 80, 3015 CN, Rotterdam, The Netherlands

Received January 21, 2019; Revised June 18, 2019; Editorial Decision July 02, 2019; Accepted July 10, 2019

ABSTRACT

The majority of the proteins involved in processing of DNA double-strand breaks (DSBs) accumulate at the damage sites. Real-time imaging and analysis of these processes, triggered by the so-called microirradiation using UV lasers or heavy particle beams, yielded valuable insights into the underlying DSB repair mechanisms. To study the temporal organization of DSB repair responses triggered by a more clinically-relevant DNA damaging agent, we developed a system coined X-ray multi-microbeam microscope (XM3), capable of simultaneous high dose-rate (micro)irradiation of large numbers of cells with ultra-soft X-rays and imaging of the ensuing cellular responses. Using this setup, we analyzed the changes in real-time kinetics of MRE11, MDC1, RNF8, RNF168 and 53BP1—proteins involved in the signaling axis of mammalian DSB repair—in response to X-ray and UV laser-induced DNA damage, in non-cancerous and cancer cells and in the presence or absence of a photosensitizer. Our results reveal, for the first time, the kinetics of DSB signaling triggered by X-ray microirradiation and establish XM3 as a powerful platform for real-time analysis of cellular DSB repair responses.

INTRODUCTION

DNA double-strand breaks (DSBs) are arguably the most severe and dangerous DNA lesions—unrepaired DSBs can cause cell death, while their incorrect repair can result in potentially carcinogenic genome rearrangements. Cells have, therefore, evolved complex mechanisms to detect, signal and repair DSBs in a timely, precise and efficient manner. In mammalian cells, direct detection of broken DNA ends is attributed to the MRE11–NBS1–RAD50 (MRN) complex (1), which then attracts and activates the ataxia-telangiectasia mutated (ATM) kinase (2), as well as the KU complex, which enables binding and activation of the DNA-PK kinase (3). Both kinases in turn phosphorylate the C-terminal serine of histone H2AX in the vicinity of DSBs (4,5). Phosphorylated H2AX (referred to as γH2AX) is recognized and bound by MDC1, which becomes phosphorylated by ATM, attracting the E3 ubiquitin ligase RNF8 (6–8). The subsequent RNF8-mediated ubiquitination of the linker histone H1 (9) engages another ubiquitin ligase, RNF168, which deposits additional ubiquitin moieties on the surrounding H2A-type histones (10), stimulating the binding of the BRCA1 complex and 53BP1. These latter components of DSB signaling compete to determine the choice of downstream repair pathway: while BRCA1 promotes the resection of DNA ends that is required for initiation of homologous recombination (HR), 53BP1 inhibits BRCA1, promoting non-homologous end joining (NHEJ) (11).

Binding of these and many other proteins involved in DNA repair to DNA lesions or to the adjacent chromatin has been extensively studied over the last two decades. The method of choice in these studies, called microirradiation, involves induction of large amount of DNA lesions concentrated in a small area of the cell nucleus, usually with the help of various high-intensity laser beams, which is then followed by real-time imaging to quantify the accumulation

*To whom correspondence should be addressed. Tel: +31 205 668 746; Fax: +31 206 974 156; Email: p.krawczyk@amsterdamumc.nl

of fluorescently-tagged repair proteins in this region (12). Studies based on this approach have provided valuable insights into the spatio-temporal organization of DNA repair processes and the underlying molecular mechanisms (12). However, it is increasingly clear that the accumulation kinetics of many proteins can be affected by the choice of the microirradiation method (13–15) or by other experimental parameters such as the type and amount of induced lesions, the cell line used or the presence of a photosensitizer (16). Importantly, at least some cellular responses are saturated at relatively low damage doses (17) and can be triggered, possibly with different kinetics, by different DNA lesions (e.g. DSBs and UV-induced damage) (18).

To overcome these problems, we constructed a live-cell microscopy system that is capable of irradiating cells with ultra-soft X (USX)-rays and of real-time imaging of the ensuing cellular responses. Using this system, we performed a comprehensive analysis of the behavior of proteins involved in DSB signaling (MRE11, MDC1, RNF8, RNF168 and 53BP1), in response to USX-ray- and UV laser-induced DNA lesions. The results of this analysis show distinct accumulation kinetics of some proteins after local USX and UV laser microirradiation, in the presence or absence of the photosensitizer Hoechst, as well as in non-cancerous (ARPE-19) and cancer (U2OS) cells.

MATERIALS AND METHODS

Plasmids

Human *MRE11* (NM_001330347.1), *RNF8* (NM_003958.3), *RNF168* (NM_152617.3) and *53BP1* (NM_001141980.2) were cloned from ARPE-19 cDNA mix. Human *MDC1* (NM_014641.2) was cloned from MDC1 in pENTR4 (330-5) vector obtained from Dr Eric Campeau (Addgene plasmid # 26427). The appropriate PCR products generated using Q5 High-Fidelity DNA Polymerase (New England Biolabs) were cloned into pAZ096-CN7 (*MDC1, MRE11*, *RNF8*, *53BP1*), pAZ096-CC7 (*RNF168*) or pAZ096-RC7 (*53BP1*) piggyBac vectors with sequence- and ligation-independent cloning (SLIC) protocol (19) using XhoI restriction site and T4 DNA polymerase (New England Biolabs). Obtained vectors allow for expression of N- or C-terminally tagged proteins fused in frame with green fluorescent protein Clover (pAZ096-CN7 and pAZ096-CC7) or red fluorescent protein mRuby2 (pAZ096-RC7). All primers used in this study are listed in Supplementary Table S1. Expression vectors are available from the authors upon request.

The pAZ096 piggyBac and mPB vectors were kind gifts from Dr Alex N. Zelensky. In brief, pAZ096 piggyBac vector was derived from 5′-PTK-3′ vector (20) by replacing the transposon cargo (XhoI-SpeI fragment) with two expression cassettes: loxP-flanked PGK-puro-SV40 poly A and CAG-[XhoI/ClaI]-BGH poly A (bovine growth hormone polyadenylation signal). The pAZ096 piggyBac vector was further modified by inserting Clover or mRuby2 cDNA between CAG promoter and Xho/ClaI restriction sites allowing adding the fluorescent tag either at N- (pAZ096-CN7) or C-terminus (pAZ096-CC7 and pAZ096-RC7) of protein of interest. Clover and mRuby2 cDNA were cloned from pcDNA3-Clover and pcDNA3-mRuby2 vectors, respectively, acquired from Dr Michael Lin (Addgene plasmid #40259). mPB vector coding for piggyBac transposase was described by Cadiñanos and Bradley (20).

All plasmids used in transfections were propagated in chemically competent DH5α *Escherichia coli* and purified using NucleoBond Xtra Midi kit (Macherey-Nagel). Each expression construct was verified by Sanger sequencing (BaseClear).

Cell culture and transfections

ARPE-19 (human retinal pigmented epithelium, ATCC, CRL-2302) and U2OS (human osteosarcoma, ATCC, HTB-96) cells were cultured in DMEM with 4.5 g/l D-glucose, 1 mM sodium pyruvate and 4 mM L-glutamine (Gibco, Life Technologies) supplemented with 100 units/ml of penicillin G (Gibco, Life Technologies), 100 μg/ml of streptomycin (Gibco, Life Technologies) and 10% (v/v) fetal bovine serum (Gibco, Life Technologies). Normal human skin fibroblasts (a kind gift from Dr Alex Postma, Department of Clinical Genetics, Amsterdam University Medical Centers, Amsterdam, The Netherlands), SV40-transformed XP2OS fibroblasts from an XPA-deficient patient stably expressing XPA-GFP (21) and SV40-transformed XP4PA fibroblasts from XPC deficient patient stably expressing XPC-GFP (22) were cultured in RPMI 1640 Medium with 2 mM L-glutamine (Gibco, Life Technologies) supplemented as above. XR-V15B cells stably expressing KU80-EGFP and V3 cells stably expressing DNA-PKcs-YFP (obtained from Dr Dik van Gent) were cultured in MEM with 2 mM L-glutamine (Gibco, Life Technologies) supplemented as mentioned above. Cells were maintained at 37°C in humidified atmosphere with 5% CO_2.

Transfections were performed using GenJet Plus reagent (SignaGen Laboratories) according to the manufacturer's instructions. Briefly, ARPE-19 or U2OS cells were plated 24 h prior to transfection in a 60 mm dish and the following day were co-transfected with 1.5 μg of an expression vector and 1.5 μg mPB vector. Two days after transfection, cells were passaged into a 100 mm dish in medium containing 0.5 μg/ml puromycin (Gibco, Life Technologies) as selection antibiotic. Cells were selected for 3 weeks. After selection cells were sorted using a Sony SH800Z cell sorter with 100 μm sorting chip. Established stable cell lines were continuously maintained in medium containing 0.5 μg/ml puromycin. In case of SV40-transformed fibroblasts, the cells were plated 24 h prior to transfection in a 60 mm dish, transfected the following day with 3 μg of of 53BP1-Clover or 53BP1-mRuby2 vectors and 24 h later plated for experiments as described below in (Micro)irradiation and image acquisition section.

Characterization of the XM3 USX-ray source

The XM3 USX-ray source emission spectrum measurements were performed using a SiriusSD silicon drift detector (SGX Sensortech) coupled to a DX200 digital pulse processor (SGX Sensortech). Spectral data were processed using SGX1000 software (SGX Sensortech). Photon flux

was analysed using DXP counter (AMOLF). UV spectral energy output was measured using a Model 550-1 radiometer/photometer (EG&G Electro-Optics) equipped with a 550-2 multiprobe (EG&G Electro-Optics) and appropriate filter sets (Schott).

(Micro)irradiation and time-lapse imaging

For (micro)irradiation, 1×10^6 cells were plated into a custom-made culture dish with a 4 μm polypropylene (LGC) bottom 24 h before experiments. To promote proper cell attachment and spreading, the dishes were carbon-coated prior to use according to protocol described previously (23). One hour before (micro)irradiation and imaging, the culture medium was replaced with FluoroBrite DMEM (Gibco, Life Technologies) supplemented as mentioned in Cell culture and transfections section. For experiments in the presence of a photosensitizer, Hoechst 33342 (Sigma-Aldrich) was added to FluoroBrite DMEM at a final concentration of 1 μg/ml 30 min prior to irradiation. To prevent evaporation, the culture medium was overlaid with mineral oil (Sigma-Aldrich). During (micro)irradiation and image acquisition, cells were maintained at 37°C in an atmosphere with 5% CO_2. All (micro)irradiation experiments (except UV-microirradiation experiments shown in Supplementary Figure S2) were performed using the XM3 system. XM3 system and USX-ray (micro)irradiation details are described in the main text (Results section). Time-lapse imaging was carried out using a 63x dipping lens objective (HCX APO L 63x/0.90 W U-V-I CS2, Leica Microsystems) with the confocal pinhole set at 1 Airy unit (156.04 μm). Cells were imaged using an argon laser (488 nm laser line, LASOS Lasertechnik, model LGK 7872 ML05). Images were acquired as single *Z*-planes. For quantitative and comparative imaging, identical image acquisition parameters were used for each set of experiments. The exact time-lapse intervals are indicated in the figure legends.

For induction of local UV damage, normal human skin fibroblasts were grown on coverslips, washed with 1× PBS, covered with a polycarbonate filter with 5 μm-diameter pores (Millipore), irradiated with 80 J/m^2 (overall dose) using an UV-C lamp and incubated in standard growth medium for 30 min before fixation and staining.

For experiments requiring irradiation of cells with γ-rays, a ^{137}Cs source providing a dose rate of approximately 0.5 Gy/min was used.

Analysis of (micro)irradiation time-lapse data

2D microirradiation time-lapse data were analyzed according to guidelines described previously (16). Image analysis was performed using ImageJ 1.51s (24). Briefly, single cells were cropped from time-lapse sequences and registered using StackReg plugin (25) with rigid body transformation to compensate for cell movement during acquisition. The average fluorescence intensity was then measured in a circular, 3 μm-diameter region of interest for all recorded time points. For each individual cell, the fluorescence intensity at the initial time point was subtracted from all subsequent intensity data, resulting in the lower bound normalized to 0. Next, the upper bound of all intensity data was normalized to 1. After normalization, a custom-written MATLAB (MathWorks) script was used to fit one parameter second-order exponential curves (26) to all collected datasets. Based on the fitted curves, the time required for the normalized fluorescence intensity to reach 50% and 95% of its maximal value (t_{50} and t_{95}, respectively) was calculated.

Final image adjustments (for presentation purposes only) were done using Adobe Photoshop CC Version 22.1 and Adobe Illustrator CC Version 19.1.2 (Adobe Systems).

Immunofluorescence imaging

For immunofluorescence imaging experiments a standard protocol was used. In brief, 20 min after (micro)irradiation, cell culture medium was aspirated and the cells were rinsed two times with PBS (Lonza) and subsequently fixed for 15 min in 2% (v/v) methanol-free formaldehyde (Electron Microscopy Sciences) in PBS at room temperature. Next, fixative was aspirated and the cells were rinsed three times in PBS. Specimens were then blocked and permeabilized for 30 min at room temperature in TNBS [1x PBS (Lonza), 5% (v/v) FBS (Gibco, Life Technologies), 0.1% (v/v) Triton X-100 (Sigma-Aldrich)]. Directly after blocking, cells were incubated with antibodies diluted in TNBS. γH2AX was stained with mouse anti-γH2AX (Ser139) monoclonal antibody (1:100, clone JBW301, #05-636, Upstate) and Cy3-conjugated goat anti-mouse antibody (1:100, #115-165-166, Jackson ImmunoResearch). To distinguish between S- and non-S-phase cells, Click-iT EdU staining was applied. In that case, cells were incubated with 10 μM EdU 30 min before irradiation and EdU detection was performed according to the manufacturer's recommendations using Alexa Fluor 488 dye (Thermo Fisher Scientific) before incubation with antibodies. UV damage experiments were accomplished by using the following set of antibodies: mouse anti-γH2AX (Ser139) monoclonal antibody (1:100, clone JBW301, #05-636, Upstate), rabbit anti-γH2AX (Ser139) polyclonal antibody (1:500, #ab11174, Abcam), mouse anti-CPD monoclonal antibody (1:200, #TDM-2, Cosmo Bio), rabbit anti-XPC polyclonal antibody (1:500, #A301-122A, Bethyl), rabbit anti-XPA polyclonal antibody (1:250, #FL-273, sc-853, Santa Cruz), Alexa Fluor 488-conjugated goat anti-rabbit antibody (1:2000, #A11034, Thermo Fisher Scientific), Alexa Fluor 594-conjugated goat anti-rabbit antibody (1:2000, #A11037, Thermo Fisher Scientific), Alexa Fluor 488-conjugated goat anti-mouse antibody (1:2000, #A11029, Thermo Fisher Scientific) and Alexa Fluor 594-conjugated goat anti-mouse antibody (1:2000, #A11032, Thermo Fisher Scientific). For CPD stainings, the DNA was denatured for 5 min with 0.5M NaOH before permeabilization. All incubations with primary and secondary antibodies were done for 90 or 45 min, respectively, in the dark at room temperature. In-between incubations with antibodies and after incubation with secondary antibodies, cells were washed 3 times in PBS for 5 min. Finally, all samples were mounted onto glass slides (Thermo Fisher Scientific) in Vectashield Mounting Medium with DAPI (Vector Laboratories) to counterstain nuclei and sealed with transparent nail polish.

All immunofluorescence images were acquired using a semi-motorized upright Leica DM6 B inverted wide-field fluorescence microscope (Leica Microsystems). Images were recorded with a 100× oil immersion objective (PLAN APO 100×/1.40/OIL Phaco3, Leica Microsystems) using a 16-bit 4.2 MP sCMOS monochrome Leica DFC9000 GT camera (Leica Microsystems) with Leica Application Suite X image acquisition software. The following filter sets (Leica Microsystems) were used: A for detection of DAPI (nuclei), L5 for detection of Alexa Fluor 488 dye (EdU) and Y3 for detection of Cy3 dye (γH2AX). After deconvolution from ∼30 *Z*-sections with 200 nm spacing, images were analyzed by local background subtraction and thresholding using Huygens Software (Scientific Volume Imaging). Automated γH2AX foci counting (number of γH2AX foci per nucleus) was performed using custom-written MATLAB script. Final image adjustments (for presentation purposes only) were done as mentioned earlier.

Confocal fluorescence recovery after photobleaching (FRAP)

FRAP experiments were performed using XM3 system setup. Imaging was carried out using a 63x dipping lens objective (HCX APO L 63×/0.90 W U-V-I CS2) (Leica Microsystems) at 10× digital zoom with the confocal pinhole set at 1 Airy unit (156.04 μm) and active FRAP booster. Image size was set at 128 × 40 pixel (23.43 × 7.20 μm) with 600 Hz scanning speed (bidirectional X, pixel dwell time 3.25 μs). The 128 × 40 pixel window contained a smaller circular bleach region of interest (ROI, 3 μm in diameter) placed over the DSB-containing area or the undamaged nucleoplasm as indicated in figure legends. Cells were imaged and bleached using an argon laser (488 nm laser line) (LASOS Lasertechnik, model LGK 7872 ML05). Laser powers for pre-bleach and post-bleach imaging were maintained below 40 μW, while bleaching was performed at 1.6 mW. Actual laser powers were measured at the focal plane of the objective using Ophir Vega Power and Energy Meter with PD300-CIE sensor (Ophir Photonics). After 2 pre-bleach scans of the entire scanning area, bleaching ROIs were scanned (bleached) 10 times. During recovery, images were recorded every 0.5 s for 10 s (20 images in total) followed by a series of images collected every 1 s for 50 s (MRE11, RNF8, RNF168) or 110 s (MDC1, 53BP1) resulting in 60 or 120 s of imaging in total, respectively. Pre-bleach and post-bleach images were acquired with no line averaging. FRAP data analysis, including corrections for background and photobleaching, curve fittings and half time-time of recovery and diffusion coefficients, was performed as described previously (27).

Scanning electron microscopy

The XM3 10 μm-thick nickel masks were imaged using a Zeiss Sigma 300 scanning electron microscope. As masks are made of metal, no specimen preparation was needed prior to imaging.

The imaging conditions were: working distance 5.0–6.2 mm, accelerating voltage 10 kV, aperture size 30 μm and image resolution of 2048 × 1536.

Western blot analysis

Equal numbers (400 000) of ARPE-19 and U2OS cells expressing Clover-RNF8 were lysed in RIPA buffer (25 mM Tris–HCl pH 7.6, 150 mM NaCl, 1% NP-40, 1% sodium deoxycholate, 0.1% SDS with Complete ULTRA protease inhibitors (Roche) and 1 mM PMSF (Sigma-Aldrich)) and equal volumes of cell lysates were analyzed by Western blot. Following antibodies were used: anti-GFP tag (1:3000, #A11122, Thermo Fisher Scientific), anti-β-actin (1:1000, #4970, Cell Signaling Technology) and anti-rabbit HRP (1:5000, #7074, Cell Signaling Technology). Luminescence was detected using Clarity Western ECL Substrate (Bio-Rad) and recorded using the Fusion-Fx documentation system (Vilber Lourmat).

Flow cytometric analysis

Equal numbers of ARPE-19 and U2OS cells expressing Clover-RNF8 (200.000 of FSC/SSC gated cells/sample) were analyzed for Clover fluorescence intensity by flow cytometry using the BD FacsCanto cytometer (Becton Dickinson). BD CellQuest Pro software (Becton Dickinson) was used for data acquisition and the comparison of Clover fluorescence intensity was prepared using the FlowJo software (v10.6, FlowJo).

Statistical analysis

All graphs and statistical analyses were done using GraphPad Prism (version 7.03, GraphPad Software). Additional statistical tests information is described in the figure legends. The number of replicates for each experiment is indicated in the figure legends.

RESULTS

Microirradiation system for real-time imaging of cellular responses to USX-ray-induced DNA damage

Since many repair proteins (e.g. KU, PARP1) accumulate at DNA lesions within seconds after damage induction, a universal system for real-time imaging of repair responses should ideally induce well-defined type(s) of DNA lesions at high dose-rates and be capable of imaging cellular responses before and immediately after irradiation. Therefore, we developed the X-ray Multi-Microbeam Microscope (XM3), which relies on the previously described USX-ray source (28) (Figure 1A and B). The system is vertically oriented, with the aperture of the USX source positioned directly under the sample holder of a customized Leica TCS SP5 II upright confocal microscope, equipped with a 37°C and CO_2 incubator, resonant scanner for fast imaging and 63× water-dipping objective. For uniform and simultaneous irradiation of large cell populations, custom-made culture dishes with cells growing on a 4 μm polypropylene bottom are positioned on the sample holder with hexagonally-distributed circular openings, each with a diameter of 2 mm, which determine the irradiated area of the cell culture dish (Figure 1B and C). For microirradiation experiments, a 10 μm-thick nickel micro-aperture filter (see below for detailed description) is additionally inserted between the sample holder and

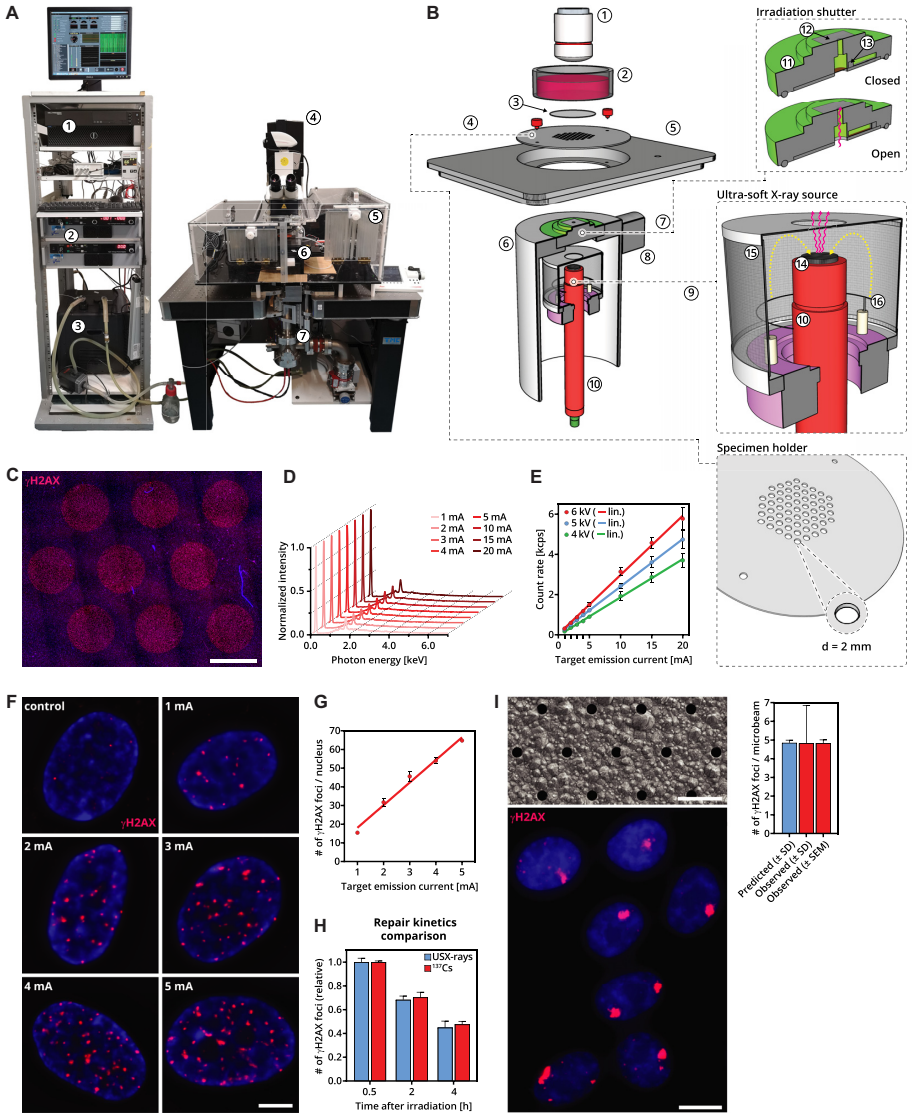

Figure 1. The ultra-soft X-ray multi-microbeam microscope (XM3). (**A**) The main components of the XM3 system are: control PC (1), power supplies (2), water cooling system (3), Leica TCS SP5 II upright confocal microscope (4), custom-made incubator (5), microscope stage (6) and the ultra-soft X (USX)-ray source assembly (7). (**B**) Schematic representation of the microscope stage assembly and USX-ray source, composed of the water-dipping 63x objective (1), cell culture dish with 4 μm polypropylene bottom (2), nickel micro-aperture filter (used during microirradiation experiments) (3), specimen holder with an array of 2-mm circular openings through which cells are irradiated (4), custom-made microscope stage inlay (5), stainless steel vacuum enclosure (6), electromagnetic irradiation shutter (7), electromagnet (8), USX-ray source (9) and water-cooled target mount (10). The irradiation shutter is composed of a CNC-machined aluminum disc (11) with aluminium-coated 4 μm polypropylene vacuum window (12) and a small neodymium magnet connected to a copper plate with a 2 mm circular aperture (13). The shutter is operated by changing the polarity of the electromagnet (8). The USX-ray source is composed of a carbon disc target (anode, 14) placed on top of the water-cooled target mount (10). The electrons (yellow dashed arrows) are produced by thermionic effect from a tungsten filament (16) heated by an electric current and focused on the anode by the focusing cage (15). USX-rays are depicted as purple arrows. (**C**) XM3 allows simultaneous irradiation of large cell numbers. ARPE-19 cells were irradiated through the specimen holder openings (10 s, 6 kV, 5 mA, without using the micro-aperture filters), fixed 20 min after irradiation and stained for DNA (blue) and γH2AX (red). Each circular γH2AX-positive area contains hundreds of uniformly-irradiated cells. Scale bar: 2 mm. (**D**) XM3 emission spectrum is independent of the emission current. The graph shows normalized energy spectra of photons produced by XM3 at the acceleration voltage of 6 kV and the indicated emission current (1–20 mA). Note the principal carbon K-shell emission line at ∼280 eV. (**E**) The flux of USX-ray photons emitted by XM3 (measured as kilo counts per s, kcps) linearly depends on the emission current. $N = 3$, error bars: SD. (**F**) Representative images of individual normal human fibroblasts irradiated and processed as in (C) but using the indicated emission current. Scale bar: 5 μm. (**G**) The number of DSBs (determined by counting the number of γH2AX foci in irradiated normal human fibroblasts) induced by XM3 linearly depends on the emission current. Cells were irradiated and processed as in (F). Data points: average from independent three experiments at ∼100 cells per experiment. Error bars: SD. (**H**) Repair of DSBs induced by XM3 and γ-rays proceeds with similar kinetics. Bars represent the average number of γH2AX foci in normal human fibroblasts fixed at the indicated time after irradiation using either XM3 (6 kV, 2.5 mA, 0.5 s) or ^{137}Cs source (2 Gy) and fixed at the indicated time points. Data points: average from three independent experiments at ∼100 cells per experiment. Error bars: SD. (**I**) Micro-aperture filters enable simultaneous microirradiation of large cell numbers. Top-left: scanning electron microscope image of the surface of the circular micro-aperture filter (element #3 in the schematic representation (B)). Bottom: representative image of ARPE-19 cells irradiated using the XM3 (6 kV, 5 mA, 10 s) equipped with the circular micro-aperture filter, fixed 20 min later and processed as in (F). Top-right: the number of γH2AX foci per microirradiated area predicted from (G) corresponds to the detected foci number. Data points: average from ∼180 cells. Scale bars: 10 μm.

the culture dish. Positioning of the USX-ray source along the optical axis of the microscope, directly below the lens, allows simultaneous irradiation of a 2 mm-diameter area and fluorescence imaging of irradiated cells.

Analysis of the USX-ray source emission spectrum showed the expected principal carbon K-shell (C_K) emission line at ∼280 eV, as well as the broadly distributed bremsstrahlung radiation whose upper energy bound is determined by the 6 kV accelerating voltage of the focussing cage (Figure 1D). If needed, XM3 may be also operated at lower (2–5 kV) accelerating voltage of the focussing cage (Supplementary Figure S1A and B). The contribution of bremsstrahlung photons (energies between 0.8 and 6 keV) to the total photon flux is ∼2.6-fold larger than the contribution of the principal carbon peak. XM3 produces only trace amounts of VIS- and UV-range photons (Supplementary Figure S2A**)** which are likely emitted by the glowing filament (electron source) and reflected off the walls of the vacuum enclosure. Further, no UV-specific DNA photolesions could be detected in USX-microirradiated cells as revealed by immunostaining for cyclobutane pyrimidine dimers and for nucleotide excision repair proteins XPA and XPC (Supplementary Figure S2B-D). Additionally, no accumulation of CPD photolyase, XPA or XPC was detected in microirradiated areas in living cells (Supplementary Figure S3).

To establish the rate of DSB induction during USX-irradiation, we quantified the number of γH2AX foci—generally accepted DSB markers (29,30)—in uniformly-irradiated, early-passage normal human skin fibroblasts (Figure 1F). The results showed that foci numbers increase linearly with the USX-ray source emission current up to ∼65 foci per cell (Figure 1F, G and Supplementary Figure S1C), which is the maximal foci number that can be reliably resolved using our imaging setup, due to the optical merging of adjacent foci at higher doses. Since photon flux is linearly proportional to the emission current (Figure 1E), the maximum dose-rate of the XM3 setup at emission current of 40 mA is ∼1000 DSBs/cell/s, corresponding to approximately 40 Gy/cell/s of ^{137}Cs γ-rays. Importantly, the disappearance of USX-ray-induced γH2AX foci proceeded with kinetics that was nearly identical to that after exposure to ^{137}Cs γ-rays (Figure 1H), suggesting that the rate of repair of DSBs induced by both radiation types is similar.

Among the critical components of XM3 is the 10 μm-thick nickel mask with 2.5 μm-diameter, hexagonally-distributed micro-apertures (Figure 1I). When positioned directly under the cell culture dish, this mask enables simultaneous microirradiation of subnuclear volumes of cells in a ∼3 mm^2 area of the cell culture dish (Figure 1I). Alternatively, a slit-shaped micro-aperture filter can be employed, resulting in striped irradiation patterns (Supplementary Figure S1D). To determine the number of DSBs induced in the cylindrical volumes of the cell nuclei located above the circular micro-apertures, we quantified the numbers of γH2AX foci induced in cells microirradiated at low USX-ray dose. We found that the rates of foci induction during microirradiation were comparable to rates measured during uniform irradiation, after accounting for the microirradiated volume (Figure 1I). At the moderate source emission current of 20 mA, routinely used throughout this study, 2 s micro-irradiation thus produces, on average, ∼38 DSBs in each microirradiated area. These emissions and exposure durations were sufficient for inducing measurable accumulation of multiple DSB repair proteins (Figure 2 and Supplementary Movie S1). Moreover, at emission current settings of 40 mA we could also image accumulation of the early-responding DSB repair proteins KU80 and DNA-PK (Supplementary Movie S2 and S3), even though they were not further analyzed in the current study. Combined, these results establish XM3 as a flexible, high-dose-rate platform for (micro)irradiation of mammalian cells using USX-rays and fluorescence imaging of the ensuing cellular responses.

The sequence of protein accumulation at USX-microirradiated sites does not reflect their known functions in DSB signaling

Our previous meta-analysis showed that the sequence of enzymatic events at DSB sites cannot be easily inferred from the published data on the accumulation kinetics of repair proteins after microirradiation (16). This is largely due to the considerable discrepancies in the data generated by different groups, which can be at least partly attributed to differences in experimental design, and especially to different microirradiation methods and sensitizers employed. To analyze the accumulation of DSB signaling proteins under uniform experimental conditions and in response to well-defined lesions, we generated a panel of the non-cancerous, human, retinal pigmented epithelial (ARPE-19) cell lines that stably express MRE11, MDC1, RNF8, RNF168 and 53BP1 fused, via a flexible linker, to Clover (a bright, monomeric and stable variant of the green fluorescent protein) (31). We USX-microirradiated these cells, imaged them for 30 min after irradiation (first 10 min at 10 s intervals and subsequent 20 min at 60 s intervals, Supplementary Movie S1) and analyzed the accumulation kinetics by quantifying the changes in fluorescence intensity in the irradiated areas (Figure 2A-C).

We anticipated that both the time of accumulation onset and accumulation duration (the time elapsed between the onset and maximal accumulation) of these proteins would reflect their known function in DSB repair. However, we found a similar time of accumulation onset for MRE11, MDC1, RNF8 and RNF168 and a clear, ∼40–50 s delay in the onset of 53BP1 accumulation (Figure 2B, C and Supplementary Figure S4B). Further, we found that the ubiquitin ligases RNF8 and RNF168 were first to reach—nearly simultaneously—50% of their maximal accumulation (t_{50}), followed by MRE11, MDC1 and 53PB1 (Figure 2B and C). This may be surprising because accumulation of RNF8 is known to be conditional on binding of MDC1 to phosphorylated H2AX (32). Moreover, while MRE11 has been proposed to be among the first proteins to recognize broken DNA ends, its accumulation after USX-microirradiation was relatively slow. Interestingly, in spite of the initial delay, 53BP1 reached t_{50} within time that was comparable to MRE11 and MDC1. In summary, even though our microirradiation experiments have been performed using a well-controlled system of DSB induction and under the same experimental conditions, the results present a picture of DSB

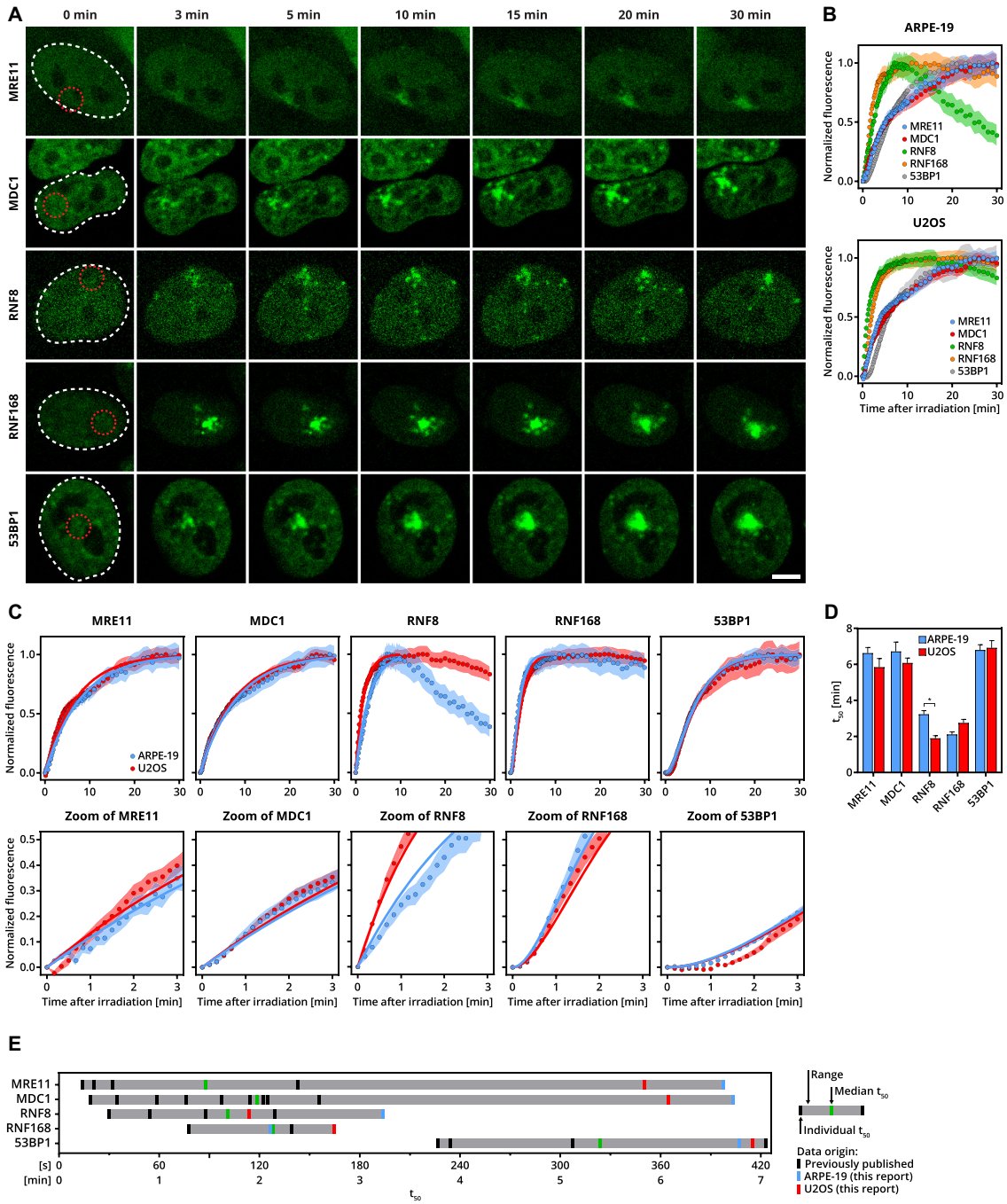

Figure 2. The kinetics of accumulation of DSB signaling proteins in USX-microirradiated areas. (**A**) DSB signaling proteins accumulate in USX-microirradiated areas. ARPE-19 cells stably expressing the indicated proteins fused to the GFP derivative Clover were microirradiated using XM3 (6 kV, 20 mA, 2 s, corresponding to an average of ∼38 DSBs per microirradiated area) and imaged at the indicated time intervals. The dashed lines mark the borders of cell nuclei (white) and microirradiated areas (red). (**B**) Cells described in (A) and identically treated U2OS cells stably expressing the same panel of proteins (see Supplementary Figure S4) were imaged for 10 min at 10 s intervals and then for 20 min at 60 s intervals. Next, images were stabilized to eliminate the cell drift and fluorescence intensity at microirradiated areas was quantified. Graphs show relative increase of fluorescence intensity, representing accumulation of the indicated proteins, at USX-microirradiated areas, over time. Top: ARPE-19 cells, bottom: U2OS cells. Data points: average normalized fluorescence intensity measured from at least 25 cells from at least three independent experiments. Shaded area: SEM. (**C**) The accumulation kinetics of RNF8 at USX-microirradiated areas differs in ARPE-19 and U2OS cells. Top: comparison of the accumulation kinetics of individual proteins in ARPE-19 and U2OS cells (data from (B)). Bottom: zoom in on the first 3 min of accumulation kinetics from the respective top panels. Data points: average normalized fluorescence intensity measured from at least 25 (ARPE-19) or 30 (U2OS) cells. Shaded area: SEM. Solid lines: fit to data. (**D**) The graph represents the time required for half-maximum accumulation (t_{50}) of the indicated protein in the indicated cell line, calculated from the fits of data shown in (C). The data were analysed using unpaired Student's *t*-test. (**E**) DSB signaling proteins are characterized by varying accumulation speeds. Comparison of accumulation speeds, expressed as half-maximum accumulation (t_{50}), of all proteins analyzed in this study to previously published data on accumulation of these proteins. Solid lines indicate individual datasets originating from previously published studies (black) or this report (blue and red, ARPE-19 and U2OS, respectively). Solid green lines indicate the median t_{50} value for each protein. Error bars: SEM. * $P = 0.011$.

signaling responses that is somewhat inconsistent with the well-described molecular mechanisms that drive them.

The accumulation kinetics of RNF8, but not other signaling proteins, differs in non-cancerous and cancer cells

While U2OS and HeLa cancer cell lines are most commonly used in microirradiation experiments (16), it is not known whether protein accumulation kinetics differs in cancer and normal human cells. To explore this question, we generated a panel of U2OS cells that express the previously discussed DSB signaling proteins and measured the kinetics of their accumulation at USX-microirradiated sites (Figure 2D and Supplementary Figure S4). We found that while the accumulation of most proteins in ARPE-19 and U2OS cells was similar, the accumulation of RNF8 differed significantly between the two cell lines, with t_{50} nearly two times longer in U2OS cells (Figure 2C–E). Moreover, the dissolution of RNF168 foci was clearly accelerated in ARPE-19, as compared to U2OS cells (Figure 2C).

The accumulation kinetics of some of the signaling proteins are considerably different at USX-ray and laser-induced DNA damage and can be affected by the photosensitizer Hoechst 33342

To compare the accumulation kinetics at X-ray and laser-induced DNA damage, we microirradiated all ARPE-19 cell lines using a commonly used 405 nm diode laser and analyzed the accumulation kinetics as described above (Figure 3A). We found that the accumulation kinetics varied substantially for MRE11 and MDC1, with t_{50} differing by over 4- and 2-fold, respectively, but was comparable for RNF8, RNF168 and 53BP1 (Figure 3B and C).

Photosensitizers such as Hoechst 33342 are commonly used in combination with laser microirradiation techniques (16) to increase the amount of induced DNA damage (33). However, the effects of Hoechst on the DSB repair responses are unknown. Analysis of the effects of Hoechst using laser microirradiation is challenging because the quantities and qualities of DNA damage induced in the presence and absence of the photosensitizer can be considerably different. However, this is not likely when Hoechst is combined with X-ray microirradiation. We therefore USX-microirradiated ARPE-19 cells in the presence of Hoechst 33342 and found that pre-incubation with the sensitizer did not induce significant changes in accumulation kinetics of the analyzed proteins. In contrast, Hoechst dramatically decreased (by over 10-fold) the accumulation t_{50} of RNF8 and, to a smaller degree (over 2-fold), increased the t_{50} of MDC1 when cells were microirradiated using the UV laser (Figure 3B and C).

The diffusion speed of DSB signaling proteins at USX-microirradiated chromatin is generally reduced, as compared to undamaged chromatin

In order to reach the damaged chromatin, repair proteins must travel through the cell nucleus and their accumulation may be dependent on, and/or limited by, their diffusion speed. We therefore measured the confocal diffusion coefficients ($D_{confocal}$) of DSB signaling proteins in undamaged nuclei and at the USX-microirradiated sites (Figure 4A and B). $D_{Confocal}$ is calculated using a simplified equation which extracts the diffusion coefficients from confocal FRAP data, using the half time of recovery and effective bleach radius for a circular bleach region (27). We found that $D_{confocal}$ of free proteins in undamaged nuclei was high for MRE11, RNF8 and RNF168, as compared to 53BP1 and MDC1, but considerably lower relative to free Clover (Figure 4C). We also measured $D_{confocal}$ at damage sites and determined the fold change in diffusion coefficient relative to undamaged nuclei, which was surprisingly low (∼0.5-fold) and not statistically significant for MDC1 and higher (∼3-5-fold) for the remaining proteins (Figure 4D and E).

DISCUSSION

Even though the kinetics of DSB damage responses has been intensively studied for over two decades, primarily using various laser and particle (micro)irradiation setups, very little is known about the early behavior of repair proteins in response to X-ray-induced DNA damage. This is primarily because few existing facilities support experiments that require X-ray (micro)irradiation and simultaneous live-cell fluorescence imaging (34,35). The XM3 setup described here, a redesigned version of our previously published instrument (28), is a flexible platform for such experiments, with a number of important advantages. First, it allows both micro- and uniform irradiation, with microirradiated areas and patterns defined by the reusable nickel micro-aperture filters (Figure 1 and Supplementary Figure S1). Second, it is capable of producing relatively high and precisely tunable photon fluxes, and generating from low numbers to over 1000 DSBs/cell/s—sufficient for observing early DSB repair events, such as accumulation of KU and DNA-PK (Supplementary Movies S2 and S3). Third, it can simultaneously irradiate hundreds of cells in an area of ∼3 mm^2 and multiple (currently up to nine, but potentially over 20) successive areas with programmable delay, which is compatible with medium-throughput imaging experiments. XM3 does not require radiation protection measures or strong laser sources, has a relatively small footprint of ∼3 m^2, including the microscope hardware, and is deployed in a regular research laboratory.

The USX-radiation produced by XM3 (∼0.28–6 kV) induces DNA damage almost exclusively via production of low-energy electrons (36), which also represent most of the energy deposition by low linear energy transfer (low-LET) radiations, including the high-energy (hard) photons. Recent simulations suggest that the higher relative biological effectiveness of USX-rays is a product of increased DSB yield per dose unit (36,37). USX-rays thus do not likely induce complex DSBs, in contrast to typical high-LET radiations such as Bragg-peak protons or heavy ions. Indeed, our results show a very similar kinetics of DSB repair, measured indirectly by quantifying dissolution of γH2AX foci, after USX and hard photon irradiation (Figure 1H), suggesting similar lesion complexity. USX-rays thus mimic some important features of clinically-relevant X-radiation; they are also safe and can be easily collimated, which is essential for microirradiation experiments.

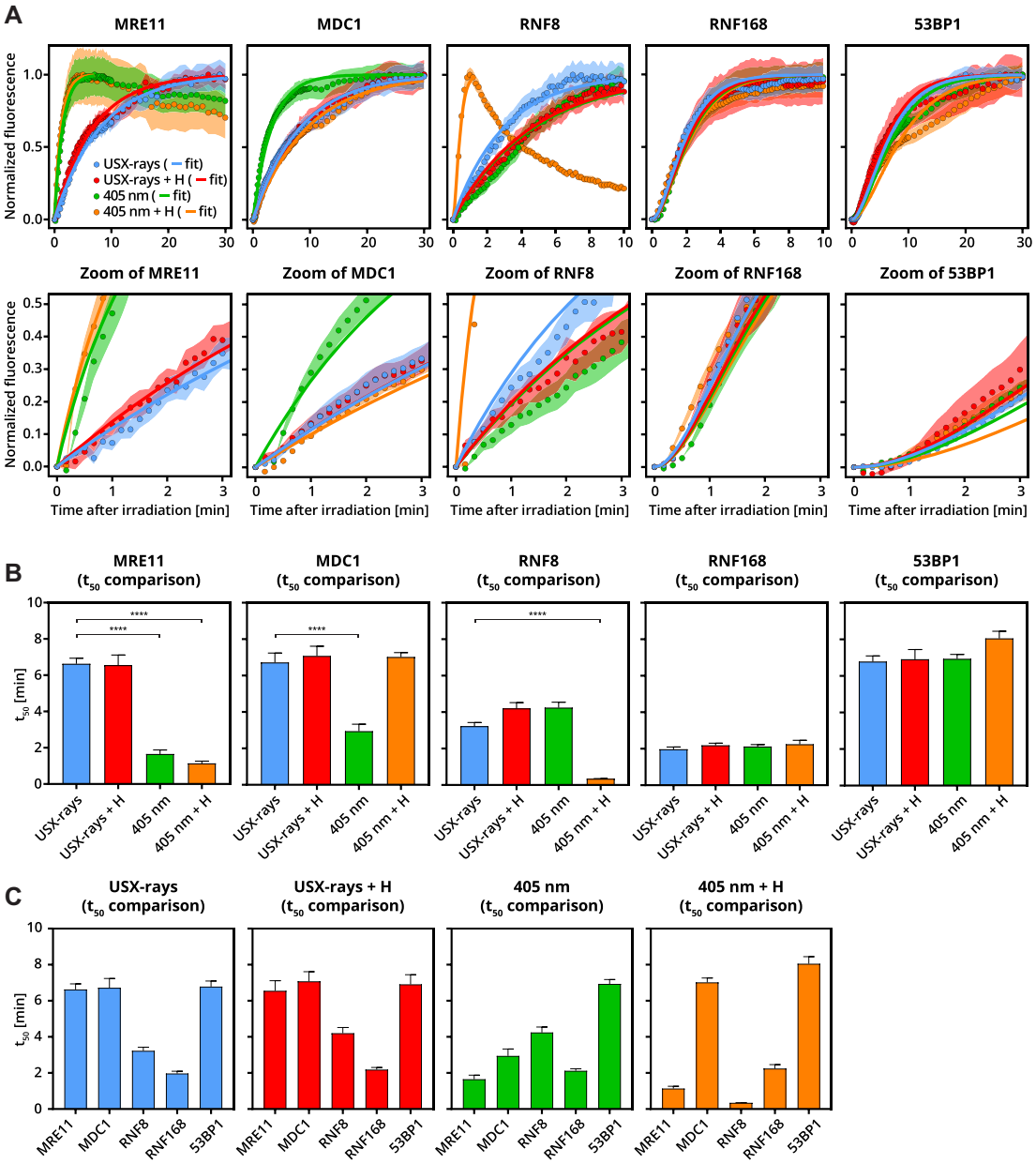

Figure 3. Comparison of the kinetics of accumulation of DSB signaling proteins at USX- and UV-microirradiated areas, in the presence or absence of Hoechst 33342. ARPE-19 cells (introduced in the legend to Figure 2), were microirradiated using XM3 or a 405 nm laser, in the presence or absence of the photosensitizer Hoechst 33342. (**A**) Top: relative increase of fluorescence intensity, representing accumulation of the indicated proteins at microirradiated areas, over time. Bottom: zoom in on the first 3 min of accumulation (data from the respective top panels). Data points: average normalized fluorescence intensity measured from at least 20 cells (for MRE11) or 25 cells (for the remaining proteins). Error bars: SEM. (**B** and **C**) Time required for half-maximum accumulation (t_{50}) for the indicated protein/condition, calculated from the fits of data shown in (A), grouped by protein (B) or condition (C). **** $P <$ 0.0001.

Multiple studies characterized accumulation of DSB signaling proteins using various laser- and particle-microirradiation approaches (16). Relative to the median reported in these studies, we found a considerably increased t_{50} of MRE11 (~4-fold) and MDC1 (~3 fold) after USX-microirradiation, while t_{50} of RNF8, RNF168 and 53BP1 were more similar to those reported by others (Figure 2E). Interestingly, a similar pattern was observed in our own comparison of USX- and UV-laser microirradiation with or without Hoechst (Figure 3), suggesting that the kinetics of accumulation of some repair proteins at microirradiated sites may be less dependent on lesion complexity, density and/or load. The large difference in the accumulation and disassembly of RNF8 at laser-microirradiated areas in the presence of Hoechst suggests that this photosensitizer may affect the kinetics of DSB repair responses by modulating lesion load and/or complexity because this effect was not recapitulated after USX-microirradiation. This result, together with clearly altered kinetics of MRE11 after laser and USX-microirradiation, confirm the earlier reports that

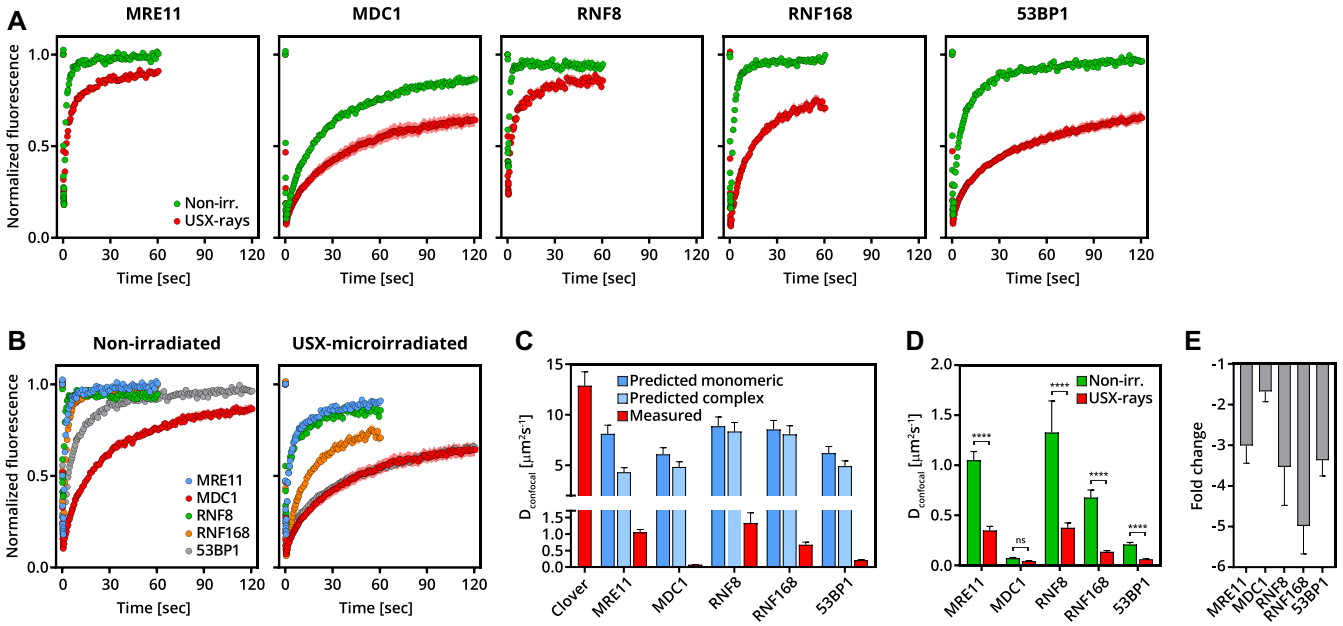

Figure 4. Comparison of diffusion speed of DSB signaling proteins in undamaged cell nuclei and at USX-microirradiated areas. (**A** and **B**) The diffusion speed of the DSB signaling proteins is reduced at DSB sites, as compared to intact nuclei. Non-irradiated or USX-microirradiated ARPE-19 cells (introduced in the legend to Figure 2) were analyzed by fluorescence-recovery after photobleaching (FRAP). Graphs represent the change in average normalized fluorescence intensity at the photobleached areas over time for each individual protein (A) or for all proteins grouped by condition (B). Data points: average from at least 20 cells per condition. Shaded area: SEM. **(C)** Comparison of theoretical confocal diffusion coefficients of all analysed Clover-tagged proteins estimated from the confocal diffusion coefficient of Clover and the molecular weight difference between pure Clover and respective tagged protein as a monomer or in the form of the largest known complex (MRE11: MRN complex, MDC1: homodimer, RNF8: with UBC13, RNF168: with RAD6, 53BP1: homodimer) as well as confocal diffusion coefficients measured in FRAP experiments in undamaged cell nuclei (calculated from the data shown in (B)). Error bars: SEM. (**D**) Confocal diffusion coefficients of the indicated proteins measured at the non-irradiated and microirradiated areas, calculated from the data shown in (B). Error bars: SEM. **** $P < 0.0001$. (**E**) Fold change of the diffusion coefficients at the microirradiated area, relative to intact nuclei (calculated from the data shown in (D)). Error bars: SEM.

accumulation kinetics may strongly depend on the chosen damage induction method (13–15) and that this effect may be protein-specific, further complicating inter-study comparisons.

Another aspect that became apparent in our previous meta-analysis (16) and has now been confirmed in direct comparisons after X-microirradiation is that the accumulation of RNF8 and RNF168 appears faster than accumulation of MRE11 and MDC1, which are known to precede the former proteins in the well-studied signaling cascade triggered by DSB induction. Intriguingly, some previous studies, including the recent comprehensive comparison of accumulation kinetics at laser-induced DNA lesions, found than the accumulation of RNF168 was generally slower than that of MDC1 (10,38). The relatively slow accumulation of MRE11 could be explained by the bi-modal interaction of this protein with the damaged chromatin: relatively few MRE11 molecules likely first interact with broken DNA ends (39), which is followed by binding of more molecules to phosphorylated histone H2AX (32). It is thus possible that the low number of DSBs that we induce at X-microirradiated areas does not allow visualizing the early recruitment but rather the later binding to γH2AX. This effect may be reflected by the clearly increased MRE11 accumulation speed after laser-microirradiation which likely induces larger quantity of DNA lesions, enabling visualization of its early recruitment phase.

When comparing the kinetics of DSB signaling responses in non-cancerous (ARPE-19) and cancer (U2OS) cells, we found that the accumulation kinetics of most proteins were nearly identical, but the accumulation and disassembly of RNF8 foci in ARPE-19 cells was clearly accelerated (Figure 2). At present, we cannot exclude that these differences are at least partly caused by different gene expression levels (Supplementary Figure S5) or other differences between these cells, including (epi)genetic makeup, tissue of origin, gene expression patterns, proliferation rates, etc. Interestingly, recent findings published by Suchankova *et al.* and Bobkova *et al.* link specific genomic alterations or cellular background with altered accumulation of proteins involved in DSB signalling (40,41). Suchankova *et al.* showed that mutations in TP53 gene affect the status of 53BP1, γH2AX and MDC1 proteins after UV-A exposure. Their results revealed that cells with different mutations in TP53 display distinct patterns of recruitment of 53BP1 protein to UVA-damaged chromatin. Moreover, TP53 mutants were found to exhibit irradiation-dependent down-regulation of MDC1 (40). Additionally, Bobkova *et al.* found that the accumulation kinetics of 53BP1 differed significantly between normal neonatal human dermal fibroblasts and U87 glioblastoma cells exposed to high-LET ^{15}N-ion radiation (41). In this context, it is likely that numerous genomic alterations present in the unstable genome of cancer (U2OS) compared to the nearly-wild type genome of the non-cancerous (ARPE-19) cells are at the roots of the distinct

accumulation and disassembly kinetics of RNF8 reported in our study.

The measured confocal diffusion speed of all analyzed proteins in non-irradiated cells appeared to be much lower than what could be predicted based on their size or on the size of their known complexes (Figure 4C); this was especially striking for 53BP1 and MDC1. Confocal diffusion speed of 53BP1 in non-irradiated cells was relatively low but decreased further (by ∼3-fold) at microirradiated sites. For MDC1, the difference in diffusion speed in intact nuclei and at and microirradiated areas was small and not statistically significant. These results suggest relatively strong interactions of these proteins with chromatin or other nuclear structures in the absence of DNA damage. Although publicly available databases such as The Research Collaboratory for Structural Bioinformatics Protein Data Bank (42) or The Biological General Repository for Interaction Datasets (43) suggest hundreds of potential interactors of proteins analysed in this report, their interactions outside of the DNA repair context remain largely unexplored. A number of studies did show, however, that 53BP1 may interact with p53, USP28, NuMA or nuclear lamins in the absence of DNA damage (44–46). Moreover, 53BP1 interactions with histone H4 methylated on lysine 20, and histone H2A ubiquitylated on lysine 15, are believed to represent an additional binding interface for 53BP1, which may be necessary for its stable chromatin association (47–49). In the case of MDC1, its interactions with APC/C subunit APC3 (Cdc27), Cdc20 and CHK2 are known to play a role in cell cycle regulation (50–52). These data may, at least to a degree, explain our observation that the diffusion speed of 53BP1 and MDC1 is much lower than expected solely on the basis of their molecular size, even in non-irradiated cells.

In summary, XM3 is a robust platform for real-time analysis of cellular responses to X-ray (micro)irradiation that can be used to study various aspects of DSB repair responses in live mammalian cells.

SUPPLEMENTARY DATA

Supplementary Data are available at NAR Online.

ACKNOWLEDGEMENTS

The authors are grateful to Dr A. Zelensky for sharing the modified piggyBAC plasmids and Dr Dik van Gent for providing the cell lines expressing fluorescently tagged DNA-PKcs and KU80.

FUNDING

Dutch Cancer Society (KWF Kankerbestrijding); Netherlands Organisation for Scientific Research (NWO). Funding for open access charge: Dutch Cancer Society (KWF Kankerbestrijding) [EMCR 2015-7846].
Conflict of interest statement. None declared.

REFERENCES

1. Lavin,M.F. (2007) ATM and the Mre11 complex combine to recognize and signal DNA double-strand breaks. *Oncogene*, **26**, 7749–7758.
2. Lee,J.-H. and Paull,T.T. (2005) ATM activation by DNA double-strand breaks through the Mre11-Rad50-Nbs1 complex. *Science*, **308**, 551–554.
3. Gottlieb,T.M. and Jackson,S.P. (1993) The DNA-dependent protein kinase: requirement for DNA ends and association with Ku antigen. *Cell*, **72**, 131–142.
4. Burma,S., Chen,B.P., Murphy,M., Kurimasa,A. and Chen,D.J. (2001) ATM phosphorylates histone H2AX in response to DNA double-strand breaks. *J. Biol. Chem.*, **276**, 42462–42467.
5. An,J., Huang,Y.-C., Xu,Q.-Z., Zhou,L.-J., Shang,Z.-F., Huang,B., Wang,Y., Liu,X.-D., Wu,D.-C. and Zhou,P.-K. (2010) DNA-PKcs plays a dominant role in the regulation of H2AX phosphorylation in response to DNA damage and cell cycle progression. *BMC Mol. Biol.*, **11**, 18.
6. Huen,M.S.Y., Grant,R., Manke,I., Minn,K., Yu,X., Yaffe,M.B. and Chen,J. (2007) RNF8 transduces the DNA-damage signal via histone ubiquitylation and checkpoint protein assembly. *Cell*, **131**, 901–914.
7. Kolas,N.K., Chapman,J.R., Nakada,S., Ylanko,J., Chahwan,R., Sweeney,F.D., Panier,S., Mendez,M., Wildenhain,J., Thomson,T.M. *et al.* (2007) Orchestration of the DNA-damage response by the RNF8 ubiquitin ligase. *Science*, **318**, 1637–1640.
8. Mailand,N., Bekker-Jensen,S., Faustrup,H., Melander,F., Bartek,J., Lukas,C. and Lukas,J. (2007) RNF8 ubiquitylates histones at DNA double-strand breaks and promotes assembly of repair proteins. *Cell*, **131**, 887–900.
9. Thorslund,T., Ripplinger,A., Hoffmann,S., Wild,T., Uckelmann,M., Villumsen,B., Narita,T., Sixma,T.K., Choudhary,C., Bekker-Jensen,S. *et al.* (2015) Histone H1 couples initiation and amplification of ubiquitin signalling after DNA damage. *Nature*, **527**, 389–393.
10. Doil,C., Mailand,N., Bekker-Jensen,S., Menard,P., Larsen,D.H., Pepperkok,R., Ellenberg,J., Panier,S., Durocher,D., Bartek,J. *et al.* (2009) RNF168 binds and amplifies ubiquitin conjugates on damaged chromosomes to allow accumulation of repair proteins. *Cell*, **136**, 435–446.
11. Escribano-Díaz,C., Orthwein,A., Fradet-Turcotte,A., Xing,M., Young,J.T.F., Tkáč,J., Cook,M.A., Rosebrock,A.P., Munro,M., Canny,M.D. *et al.* (2013) A cell cycle-dependent regulatory circuit composed of 53BP1-RIF1 and BRCA1-CtIP controls DNA repair pathway choice. *Mol. Cell*, **49**, 872–883.
12. Polo,S.E. and Jackson,S.P. (2011) Dynamics of DNA damage response proteins at DNA breaks: a focus on protein modifications. *Genes Dev.*, **25**, 409–433.
13. Dinant,C., de Jager,M., Essers,J., van Cappellen,W.A., Kanaar,R., Houtsmuller,A.B. and Vermeulen,W. (2007) Activation of multiple DNA repair pathways by sub-nuclear damage induction methods. *J. Cell Sci.*, **120**, 2731–2740.
14. Kong,X., Mohanty,S.K., Stephens,J., Heale,J.T., Gomez-Godinez,V., Shi,L.Z., Kim,J.-S., Yokomori,K. and Berns,M.W. (2009) Comparative analysis of different laser systems to study cellular responses to DNA damage in mammalian cells. *Nucleic Acids Res.*, **37**, e68.
15. Hable,V., Drexler,G.A., Brüning,T., Burgdorf,C., Greubel,C., Derer,A., Seel,J., Strickfaden,H., Cremer,T., Friedl,A.A. *et al.* (2012) Recruitment kinetics of DNA repair proteins Mdc1 and Rad52 but not 53BP1 depend on damage complexity. *PLoS One*, **7**, e41943.
16. Kochan,J.A., Desclos,E.C.B., Bosch,R., Meister,L., Vriend,L.E.M., van Attikum,H. and Krawczyk,P.M. (2017) Meta-analysis of DNA double-strand break response kinetics. *Nucleic Acids Res.*, **45**, 12625–12637.
17. Ochs,F., Somyajit,K., Altmeyer,M., Rask,M.-B., Lukas,J. and Lukas,C. (2016) 53BP1 fosters fidelity of homology-directed DNA repair. *Nat. Struct. Mol. Biol.*, **23**, 714–721.
18. Marteijn,J.A., Bekker-Jensen,S., Mailand,N., Lans,H., Schwertman,P., Gourdin,A.M., Dantuma,N.P., Lukas,J. and Vermeulen,W. (2009) Nucleotide excision repair-induced H2A ubiquitination is dependent on MDC1 and RNF8 and reveals a universal DNA damage response. *J. Cell Biol.*, **186**, 835–847.
19. Jeong,J.-Y., Yim,H.-S., Ryu,J.-Y., Lee,H.S., Lee,J.-H., Seen,D.-S. and Kang,S.G. (2012) One-step sequence- and ligation-independent cloning as a rapid and versatile cloning method for functional genomics studies. *Appl. Environ. Microbiol.*, **78**, 5440–5443.
20. Cadiñanos,J. and Bradley,A. (2007) Generation of an inducible and optimized piggyBac transposon system. *Nucleic Acids Res.*, **35**, e87.

21. Rademakers,S., Volker,M., Hoogstraten,D., Nigg,A.L., Moné,M.J., Van Zeeland,A.A., Hoeijmakers,J.H.J., Houtsmuller,A.B. and Vermeulen,W. (2003) Xeroderma pigmentosum group A protein loads as a separate factor onto DNA lesions. *Mol. Cell Biol.*, **23**, 5755–5767.
22. Hoogstraten,D., Bergink,S., Ng,J.M.Y., Verbiest,V.H.M., Luijsterburg,M.S., Geverts,B., Raams,A., Dinant,C., Hoeijmakers,J.H.J., Vermeulen,W. *et al.* (2008) Versatile DNA damage detection by the global genome nucleotide excision repair protein XPC. *J. Cell Sci.*, **121**, 2850–2859.
23. Stap,J., Van Marle,J., Van Veen,H.A. and Aten,J.A. (2000) Coating of coverslips with glow-discharged carbon promotes cell attachment and spreading probably due to carboxylic groups. *Cytometry A*, **39**, 295–299.
24. Schneider,C.A., Rasband,W.S. and Eliceiri,K.W. (2012) NIH Image to ImageJ: 25 years of image analysis. *Nat. Methods*, **9**, 671–675.
25. Thévenaz,P., Ruttimann,U.E. and Unser,M. (1998) A pyramid approach to subpixel registration based on intensity. *IEEE Trans. Image Process.*, **7**, 27–41.
26. Bekker-Jensen,S., Lukas,C., Melander,F., Bartek,J. and Lukas,J. (2005) Dynamic assembly and sustained retention of 53BP1 at the sites of DNA damage are controlled by Mdc1/NFBD1. *J. Cell Biol.*, **170**, 201–211.
27. Kang,M., Day,C.A., Kenworthy,A.K. and DiBenedetto,E. (2012) Simplified equation to extract diffusion coefficients from confocal FRAP data. *Traffic*, **13**, 1589–1600.
28. van Oven,C., Krawczyk,P.M., Stap,J., Melo,A.M., Piazzetta,M.H.O., Gobbi,A.L., van Veen,H.A., Verhoeven,J. and Aten,J.A. (2009) An ultrasoft X-ray multi-microbeam irradiation system for studies of DNA damage responses by fixed- and live-cell fluorescence microscopy. *Eur. Biophys. J.*, **38**, 721–728.
29. Rogakou,E.P., Pilch,D.R., Orr,A.H., Ivanova,V.S. and Bonner,W.M. (1998) DNA double-stranded breaks induce histone H2AX phosphorylation on serine 139. *J. Biol. Chem.*, **273**, 5858–5868.
30. Rogakou,E.P., Boon,C., Redon,C. and Bonner,W.M. (1999) Megabase chromatin domains involved in DNA double-strand breaks in vivo. *J. Cell Biol.*, **146**, 905–916.
31. Lam,A.J., St-Pierre,F., Gong,Y., Marshall,J.D., Cranfill,P.J., Baird,M.A., McKeown,M.R., Wiedenmann,J., Davidson,M.W., Schnitzer,M.J. *et al.* (2012) Improving FRET dynamic range with bright green and red fluorescent proteins. *Nat. Methods*, **9**, 1005–1012.
32. Stucki,M., Clapperton,J.A., Mohammad,D., Yaffe,M.B., Smerdon,S.J. and Jackson,S.P. (2005) MDC1 directly binds phosphorylated histone H2AX to regulate cellular responses to DNA double-strand breaks. *Cell*, **123**, 1213–1226.
33. Limoli,C.L. and Ward,J.F. (1993) A new method for introducing double-strand breaks into cellular DNA. *Radiat. Res.*, **134**, 160–169.
34. Drexler,G.A. and Ruiz-Gómez,M.J. (2015) Microirradiation techniques in radiobiological research. *J. Biosci.*, **40**, 629–643.
35. Prise,K.M. and Schettino,G. (2011) Microbeams in radiation biology: review and critical comparison. *Radiat. Prot. Dosimetry*, **143**, 335–339.
36. Buch,T., Scifoni,E., Krämer,M., Durante,M., Scholz,M. and Friedrich,T. (2018) Modeling radiation effects of ultrasoft X rays on the basis of amorphous track structure. *Radiat. Res.*, **189**, 32–43.
37. Friedrich,T., Durante,M. and Scholz,M. (2014) Modeling cell survival after irradiation with Ultrasoft X rays using the giant loop binary lesion model. *Radiat. Res.*, **181**, 485–494.
38. Aleksandrov,R., Dotchev,A., Poser,I., Krastev,D., Georgiev,G., Panova,G., Babukov,Y., Danovski,G., Dyankova,T., Hubatsch,L. *et al.* (2018) Protein dynamics in complex DNA lesions. *Mol. Cell*, **69**, 1046–1061.
39. Moreno-Herrero,F., de Jager,M., Dekker,N.H., Kanaar,R., Wyman,C. and Dekker,C. (2005) Mesoscale conformational changes in the DNA-repair complex Rad50/Mre11/Nbs1 upon binding DNA. *Nature*, **437**, 440–443.
40. Suchánková,J., Legartová,S., Ručková,E., Vojtěšek,B., Kozubek,S. and Bártová,E. (2017) Mutations in the TP53 gene affected recruitment of 53BP1 protein to DNA lesions, but level of 53BP1 was stable after γ-irradiation that depleted MDC1 protein in specific TP53 mutants. *Histochem. Cell Biol.*, **148**, 239–255.
41. Bobkova,E., Depes,D., Lee,J.-H., Jezkova,L., Falkova,I., Pagacova,E., Kopecna,O., Zadneprianetc,M., Bacikova,A., Kulikova,E. *et al.* (2018) Recruitment of 53BP1 proteins for DNA repair and persistence of repair clusters differ for cell types as detected by single molecule localization microscopy. *Int. J. Mol. Sci.*, **19**, 3713.
42. Burley,S.K., Berman,H.M., Bhikadiya,C., Bi,C., Chen,L., Di Costanzo,L., Christie,C., Dalenberg,K., Duarte,J.M., Dutta,S. *et al.* (2019) RCSB Protein Data Bank: biological macromolecular structures enabling research and education in fundamental biology, biomedicine, biotechnology and energy. *Nucleic Acids Res.*, **47**, D464–D474.
43. Oughtred,R., Stark,C., Breitkreutz,B.-J., Rust,J., Boucher,L., Chang,C., Kolas,N., O'Donnell,L., Leung,G., McAdam,R. *et al.* (2019) The BioGRID interaction database: 2019 update. *Nucleic Acids Res.*, **47**, D529–D541.
44. Gibbs-Seymour,I., Markiewicz,E., Bekker-Jensen,S., Mailand,N. and Hutchison,C.J. (2015) Lamin A/C-dependent interaction with 53BP1 promotes cellular responses to DNA damage. *Aging Cell*, **14**, 162–169.
45. Cuella-Martin,R., Oliveira,C., Lockstone,H.E., Snellenberg,S., Grolmusova,N. and Chapman,J.R. (2016) 53BP1 integrates DNA repair and p53-dependent cell fate decisions via distinct mechanisms. *Mol. Cell*, **64**, 51–64.
46. Salvador Moreno,N., Liu,J., Haas,K.M., Parker,L.L., Chakraborty,C., Kron,S.J., Hodges,K., Miller,L.D., Langefeld,C., Robinson,P.J. *et al.* (2019) The nuclear structural protein NuMA is a negative regulator of 53BP1 in DNA double-strand break repair. *Nucleic Acids Res.*, **47**, 2703–2715.
47. Fradet-Turcotte,A., Canny,M.D., Escribano-Díaz,C., Orthwein,A., Leung,C.C.Y., Huang,H., Landry,M.-C., Kitevski-LeBlanc,J., Noordermeer,S.M., Sicheri,F. *et al.* (2013) 53BP1 is a reader of the DNA-damage-induced H2A Lys 15 ubiquitin mark. *Nature*, **499**, 50–54.
48. Jorgensen,S., Schotta,G. and Sorensen,C.S. (2013) Histone H4 Lysine 20 methylation: key player in epigenetic regulation of genomic integrity. *Nucleic Acids Res.*, **41**, 2797–2806.
49. Wilson,M.D., Benlekbir,S., Fradet-Turcotte,A., Sherker,A., Julien,J.-P., McEwan,A., Noordermeer,S.M., Sicheri,F., Rubinstein,J.L. and Durocher,D. (2016) The structural basis of modified nucleosome recognition by 53BP1. *Nature*, **536**, 100–103.
50. Lou,Z., Minter-Dykhouse,K., Wu,X. and Chen,J. (2003) MDC1 is coupled to activated CHK2 in mammalian DNA damage response pathways. *Nature*, **421**, 957–961.
51. Peng,A. and Chen,P.-L. (2003) NFBD1, like 53BP1, is an early and redundant transducer mediating Chk2 phosphorylation in response to DNA damage. *J. Biol. Chem.*, **278**, 8873–8876.
52. Coster,G., Hayouka,Z., Argaman,L., Strauss,C., Friedler,A., Brandeis,M. and Goldberg,M. (2007) The DNA damage response mediator MDC1 directly interacts with the anaphase-promoting complex/cyclosome. *J. Biol. Chem.*, **282**, 32053–32064.